Polar Coordinate for Damage Imaging of Adhesively Bonded Plates Using Ultrasonic Guided Waves and Laser Doppler Vibrometer Measurements

Mohsen Barzegar, Dario J. Pasadas, Artur L. Ribeiro, Helena G. Ramos, Yevgeniya Lugovtsova, and Jannis Bulling

***Abstract*— Wavefield measurements by a scanning laser Doppler vibrometer (LDV) are generally carried out in a Cartesian coordinate. As a piezoelectric transducer generates Lamb waves following radial paths, the use of a polar coordinate can be a suitable alternative to the use of a Cartesian coordinate. Therefore, in the proposed method, using a single transducer placed on the center of the specimen, the measured wavefields are transformed into polar coordinates, making several identical radial line inspections from the center in the direction of incident waves. By taking advantage of the properties of the polar coordinates, a signal processing technique is proposed through a frequency-wavenumber filtering process in these coordinates. In this technique, by using proper filters, unwanted wave modes of the incident wave, along with all reflected waves, are filtered out. In addition, the conventional features of root-mean-square (RMS) and Euclidean distance (ED) are adapted for the polar coordinate system to image the bonded plate. The proposed signal processing and damage imaging are first introduced through a numerical simulation. Then, the performance of the proposed technique is presented by experimental measurements of two specimens, including adhesively bonded carbon fiber-reinforced plastic composite plates and bonded aluminum plates.**

***Index Terms*— Adhesive, damage imaging, disbond, nondestructive testing (NDT), scanning laser Doppler vibrometer (LDV).**

I. Introduction

HIGH strength-to-weight ratio, fatigue resistance, and damage tolerance of adhesive joints, among other properties, are the reason for the extensive usage of these structures in various industries. In fact, bonded joints are expected to tolerate static or cyclic loads for significant periods of time. These structures are, however, prone to some specific types of damage, including disbonds and voids, as well as low cohesive and adhesion strength. Therefore, nondestructive testing (NDT) for bonded joints is crucial. Existing NDT methods are still not mature enough to provide reliable inspection, as requested by most standards [1]. One of the promising candidates is based on ultrasonic waves.

The integrity of the adhesively bonded joints can be inspected by both low-frequency [2] and high-frequency [3] ultrasound. High-frequency ultrasound is expensive, may have a very short penetration depth, and may suffer under interference coming from micro-structural details [4]. On the contrary, low-frequency ultrasonic guided waves (UGWs) have the advantages of low attenuation and long propagation distance [5] and can provide a proper inspection of the structure.

Excitation and reception of ultrasonic waves, as well as UGWs, can be performed in contact using conventional ultrasonic piezoelectric transducers [6] or transducer arrays [7], or angle beam transducers [8]. To achieve a high spatial resolution, scanning with a focused high-frequency transducer in immersion is required. The main drawback of the method is that the structure is immersed in water, which may change the material properties, i.e., of polymer materials. Moreover, the sample size is limited since a big structure would require an enormous water tank. Another possibility is to use a noncontact air-coupled [9], [10], [11], or laser-based setups [12], [13], [14], [15], [16]. These techniques enable the use of dense wavefield data of the inspected structures resulting in detailed information about wavefield anomalies from interactions of waves with damages.

Using a pulsed laser scanning laser Doppler vibrometer (LDV), in which a pulsed laser is used for exciting Lamb waves at a single spot and an LDV for receiving Lamb waves, Tian et al. [17] carried out damage detections with a broadside and offside cracks in aluminum plates. To detect delamination and disbonds in an automated way, Sohn et al. [16] applied both the standing wave filter and a Laplacian image filter to recorded wavefields by LDV for composite plates. In this contribution, we mainly concentrate on a set-up that uses a piezoelectric transducer to generate UGWs and a scanning LDV to measure the wavefield across the surface of the specimen [15], [16], [18]. For more details, the reader is referred to a review [19] of possible applications of laser-based systems for NDT purposes.

Manuscript received 16 January 2023; revised 16 March 2023; accepted 29 March 2023. Date of publication 17 April 2023; date of current version 4 May 2023. This work was supported in part by the Instituto de Telecomunicações (IT) and Bundesanstalt für Materialforschung und prüfung (BAM) through the GW4SHM Project from the European Union's Horizon 2020 Research and Innovation Program through the Marie Skłodowska-Curie Funding Scheme, under Grant 860104; and in part by under Project UIDB/50008/2020. The Associate Editor coordinating the review process was Dr. Qing Wang. *(Corresponding author: Mohsen Barzegar.)*

Mohsen Barzegar, Dario J. Pasadas, Artur L. Ribeiro, and Helena G. Ramos are with the Instituto de Telecomunicações, Instituto Superior Técnico, Universidade de Lisboa, 1049-001 Lisbon, Portugal (e-mail: mohsenbarzegar.brz@gmail.com).

Yevgeniya Lugovtsova and Jannis Bulling are with the Acoustic and Electromagnetic Methods Division, Bundesanstalt für Materialforschung und -prüfung (BAM), 12205 Berlin, Germany.

Digital Object Identifier 10.1109/TIM.2023.3267528

To extract relevant features from the wavefield for damage imaging, various signal processing techniques have been proposed in the literature. Some properties are presented in terms of wave energy trapping [20], standing waves [21], and cumulative wave energy [22]. The core idea of these damage imaging techniques is based on either the interaction of UGWs with the damaged area that has lower stiffness or the energy of the trapped wave in the damaged area. Root-mean-square (RMS) and its variations are the most used criteria in this field [23], [24]. Gao et al. [25] used a multifrequency localized wave energy technique to identify delamination using UGWs. In this technique, from the interaction of propagating waves with the delamination, new wavenumber components were created, and the delamination was then identified by its localized wave energy. Radzieński et al. [26] carried out damage imaging of various types of composite plates using RMS maps and attenuation-compensated RMS maps.

Another way to image damage focuses on capturing wavenumber changes between a pristine and a damaged area. This technique is based on the estimation of the wavenumber at different points in space. Major wavenumber estimation methods are instantaneous [27] and local wavenumber mapping [28]. Segres et al. [29] presented a modified version of the local wavenumber mapping technique named self-reference broadband local wavenumber estimation (SRB-LWE). In this technique, dispersion curves corresponding to the damage-free base material are constructed from the broadband vibrational results. A passband filter bank is created based on these results in the frequency-wavenumber domain to improve the local thickness map. Lugovtsova et al. [30] compared local and instantaneous wavenumber mapping results from recorded wavefields by LDV on both sides of an aluminum-carbon fiber-reinforced plastic (CFRP) composite structure. In this study, a one-mode-one-frequency wavefield is more sensitive to delamination. Sohn et al. [16] successfully applied this technique to the image debonding of a stiffener from a composite plate.

From our experience, the application of wavenumber mapping techniques for adhesively bonded metal plates is mostly restricted because, at low frequencies, the wavenumber values of the damaged area are very close to those of the pristine regions. A high frequency used for the excitation may improve the imaging due to the excitation of higher order modes with different dispersive behaviors [31]. Then one can retain a mode of interest that is very sensitive to wavenumber changes caused by thickness variations. Using a high-frequency excitation may, however, decrease a wavelength and thus result in a very dense measurement grid, which is impractical for real applications. Another aspect concerning signal processing is related to the energy of the direct and reflected waves from the edges, which may be much higher than that of reflected waves in the damaged area, and thus, these undesired wave packets need to be filtered out [32].

Some papers suggested retrieving desired modes by applying filters in the frequency-wavenumber domain [30], [33], [34], [35]. In these papers, the 3-D wavefield data is recorded in Cartesian coordinates, and a 3-D fast Fourier transform (FFT) is applied to obtain a frequency-wavenumber response. For specimens with small dimensions and when a transducer used for excitation is within the scanning area, incident waves and waves reflected from structural boundaries overlap and need to be separated. Since they have the same wavenumber, their corresponding amplitudes in the frequency-wavenumber domain will superimpose, and it is not possible to separate them in this domain. Therefore, in these conditions and by using the 3-D FFT in the Cartesian coordinate, it is not possible to properly filter out the reflected waves, and consequently, it is not possible to obtain the image of a delamination or disbond. To circumvent the aforementioned challenges, this study proposes using polar coordinates to extract a mode that is sensitive to the damage and filter out all reflected waves coming into the scanned area.

For this purpose, the excitation source is placed at the center of the scanned area. Using a narrowband five-cycle Hanning windowed pulse for the excitation of UGWs, the wavefield is recorded by a 3-D LDV system with a dense Cartesian grid. This time domain data in Cartesian coordinates is then transformed into a polar grid using scattered interpolation. By applying a 2-D FFT over a spatial radial dimension and a temporal dimension, the frequency-wavenumber results are estimated in a polar coordinate. In this way, the 2-D spatial data in the Cartesian coordinate is reduced to the 1-D spatial data in the radial direction, which provides distinct wavenumber amplitudes of the incident and reflected waves. Retrieving the mode sensitive to thickness changes and filtering out the reflections, the data is then transformed back to the time domain using an inverse 2-D FFT. Damage imaging is carried out by selecting a proper time interval and using two adapted features of RMS and Euclidian distance (ED). In the current work, a 360° polar coordinate grid is always used. In general, the techniques presented here are also applicable to grids with an angular section, e.g., a 180° polar coordinate grid, if there is some prior knowledge of where the defect might be located. Experimental measurements of two specimens, including adhesively bonded CFRP and aluminum plates, are conducted to demonstrate the performance of the proposed method.

The remainder of the presented article is organized as follows. Section II provides a detailed explanation of the proposed method along with simulation results of an adhesively bonded aluminum plate. Section III presents the experimental set-up used to measure two specimens: one consisting of two adhesively bonded CFRP composite plates and another one of two adhesively bonded aluminum plates. Section IV shows the damage imaging results of both specimens. At last, Section V discusses the results presented and draws conclusions.

II. Method and Simulation

In part A of this section, the numerical model and results obtained using ABAQUS are presented. In part B, the signal processing in polar coordinates is explained, and in part C, the imaging process is described in detail and demonstrated on a simulated wavefield.

TABLE I
MATERIAL PROPERTIES USED IN THE SIMULATION

Material	Young's modulus [GPa]	Poisson's ratio	Density [kg/m3]
Aluminum	71	0.33	2710
Adhesive	1.65	0.40	1050

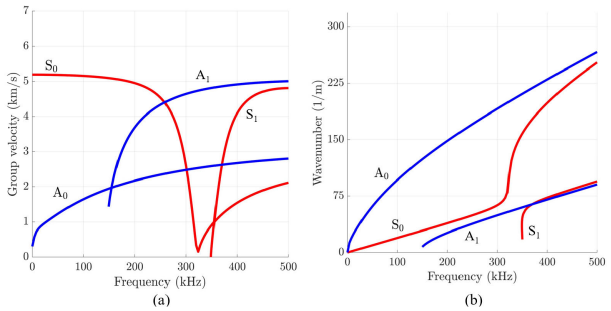

Fig. 1. Dispersion curves for the adhesively bonded sample used in the numerical model: (a) group velocities and (b) wavenumbers.

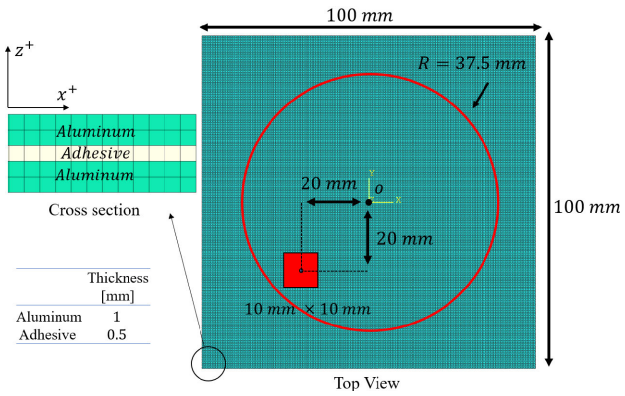

Fig. 2. Schematic of the meshed adhesively bonded aluminum plate model, disbond location, and scan area.

A. Numerical Modeling

In this study, the numerical simulation is conducted through the finite-element software package ABAQUS using the ABAQUS/Explicit solver. A detailed explanation of the numerical simulation of UGWs using ABAQUS/Explicit solver for delamination detection can be found in [36]. In the current study, a brief review of the numerical simulation of UGWs in adhesively bonded plates with artificial disbond is presented. To start with, a 3-D deformable model is created in the software with properties that are presented in Table I.

Using the mechanical properties from Table I, the dispersion curves of the bonded plate (aluminum thickness = 1 mm, adhesive thickness = 0.5 mm) are calculated by the open-source software *Dispersion Calculator* [37]. The results are presented in Fig. 1. A schematic of the meshed adhesively bonded aluminum plate model with dimensions, as well as disbond location and scan area, is depicted in Fig. 2. The model is a squared bonded plate with a side of 100 mm, and the center of the plate is considered as the origin O. The disbond, which is located at the interface of the upper aluminum plate and the adhesive has a squared shape with a side of 10 mm. To model the disbond effect, three modeled parts (two aluminum parts and one adhesive part) are bonded together (except for the disbond region) with a tie constraint in the interaction module of the software. In avoiding interpenetration of the disbond region surfaces during the wave propagation, contact acoustic nonlinearity is included [38]. This is applied by defining the surface-to-surface contact with tangential frictionless and normal hard contact behavior in the interface of disbond region. A five-cycle Hanning windowed sinusoidal pulse with a central frequency of 200 kHz is applied as a concentrated load on the origin O in the Z direction (thickness direction). According to Fig. 1, this central frequency is selected due to the proper difference of both wavenumbers and group velocities of the A0 mode compared to those of the other modes. At the frequency of 200 kHz, the wavenumber of the A0 mode is 148.35 m^{-1}, which corresponds to a wavelength of about 6.75 mm. Therefore, the wavelength is smaller than the size of disbond and detectability is ensured. The time period of the simulation is considered as 60 μs with a fixed user-defined time increment of 0.05 μs that corresponds to a sample rate of 20 MHz. To include attenuation, a damping coefficient of 0.06 is considered in the numerical process. In total, 200 000 linear hexahedral elements of type C3D8R with structured shapes are used to mesh the model. The time increment and size of elements agree with the criteria for the largest time step and element size presented in [36]. It should be noted that for a structured mesh, the distance between the opposite nodes along the diagonal of the element is the size in the criterion [39]. In this way, the largest element size in the model is about 0.87 mm. The out-of-plane displacement of the nodes on the upper surface of the plate in the scan area is recorded as a time series. These results are then passed to the next step for signal processing in the polar coordinates and imaging.

B. Signal Processing

For an excellent description of a filtering process in the frequency-wavenumber domain in the Cartesian coordinates, the reader is referred to the paper of Ruzzene [35]. The main steps are briefly presented below.

In this method, considering a propagated wavefield $v(r, t)$ with time variable t and spatial variable r, a 2-D data matrix can be obtained from the propagation of a wave on a single-line scan. Applying a fast algorithm of 2-D FFT in time and space on this matrix with respect to t and r will transform each data point into a frequency-wavenumber domain wavefield $V(k_r, \omega)$

$$V(k_r, \omega) = \int_{-\infty}^{+\infty} \int_{-\infty}^{+\infty} v(r, t) e^{-i(k_r r - \omega t)} dr dt. \quad (1)$$

In the above equation, k_r and ω are the wavenumber and frequency data, respectively. Considering a harmonic wavefield propagating with a constant radian frequency ω_0 and a constant wavenumber k_0, the wavefield with a frequency and wavenumber-dependent amplitude A_0 could be written as $v_0(r, t) = A(\omega_0) e^{i(\omega_0 t - k_0 r)}$. Thus, the transformation of this

wavefield from the time and spatial domain to the frequency-wavenumber domain through 2-D FFT is as follows:

$$V(k_r, \omega) = \int_{-\infty}^{+\infty} \int_{-\infty}^{+\infty} A_0 e^{-i(\omega_0 t - k_0 r)} e^{-i(k_r r - \omega t)} dr dt = 4\pi^2 A_0 \delta(\omega - \omega_0, k - k_0) \quad (2)$$

where, δ is a 2-D delta function. The magnitude of the $V(k_r, \omega)$ in a specific frequency $\omega = \omega_0$, has two values of $k = -k_0$ and $k = +k_0$ corresponding to the incident and reflected waves, respectively. Therefore, defining a proper filter mask in the frequency-wavenumber domain as a 2-D matrix and multiplication to the 2-D FFT results can provide filtered modes and remove the reflections. This operation is performed using the following equation to get the filtered data in the frequency-wavenumber domain:

$$V_{\text{filt}}(k_r, \omega) = V(k_r, \omega) \odot F(k_r, \omega) \quad (3)$$

where, $\odot$ denotes componentwise multiplication and $F(k_r, \omega)$ is the filter mask in the frequency-wavenumber domain. The filtered data is then transformed back into the temporal and spatial domain using the inverse 2-D FFT

$$v_{\text{filt}}(r, t) = \frac{1}{4\pi^2} \int_{-\infty}^{+\infty} \int_{-\infty}^{+\infty} V_{\text{filt}}(k_r, \omega) e^{-i(k_r r - \omega t)} dk_r d\omega. \quad (4)$$

In this article, the explained process of frequency-wavenumber filtering is applied to each line scan in the radial direction R at each angle φ. For a 3-D wavefield in a polar coordinate $v_{\text{polar}}(\varphi, r, t)$, the frequency-wavenumber filtering is applied on the two last dimensions through the 2-D FFT and the first dimension, which is the angle data that remains untouched. Therefore, this transformation to the frequency-wavenumber domain is carried out by using the following equation:

$$V_{\text{polar}}(\varphi, k_r, \omega) = \int_{-\infty}^{+\infty} \int_{-\infty}^{+\infty} v_{\text{polar}}(\varphi, r, t) e^{-i(k_r r - \omega t)} dr dt. \quad (5)$$

The remaining process of filtering is the same as what was presented for 2-D time and spatial data.

Measurements of the wavefield by an LDV system are usually conducted in a Cartesian coordinate; moreover, it is quite often a case that the space between nodes of the grid is not equal. Therefore, to have adequate accuracy in the Fourier transform, the data should either be transformed to a polar grid coordinate or carefully interpolated to make a 3-D matrix with an equal radial grid. Transforming the 3-D data in a Cartesian coordinate grid to an equally spaced polar coordinate grid can be conducted through a Delaunay triangulation of the scattered sample points [40]. Fig. 3 shows a schematic of the mesh grids in both coordinate systems with low transparency, as well as corresponding axis, grid sizes, and data points. Data points (x_i, y_j) in Cartesian coordinate $(\vec{X}, \vec{Y})$ are shown with black dots with a grid size of $(\Delta x, \Delta y)$, along with data points (φ_j, r_i) in polar coordinate $(\vec{R}, \vec{\phi})$ depicted in red dots with the grid size of $(\Delta r, \Delta \varphi)$. Using the above process, the wavefield recorded in a Cartesian form (x_i, y_j, t) is converted to a polar form (φ_j, r_i, t). Then, the proposed filtering process is applied to this polar form data.

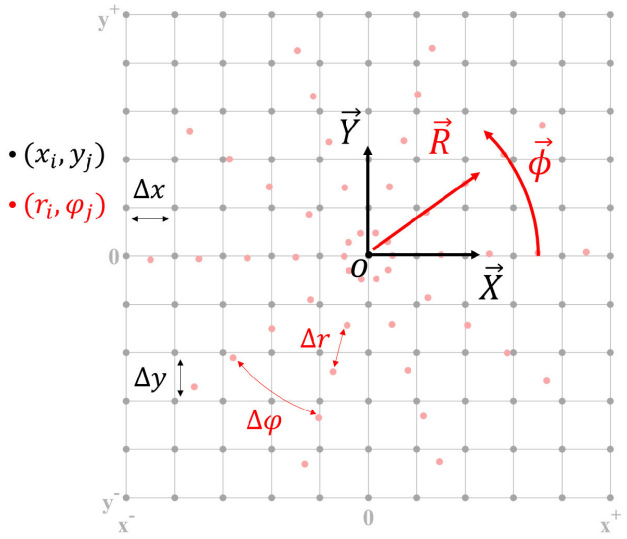

Fig. 3. Schematic of Cartesian and polar coordinate grids.

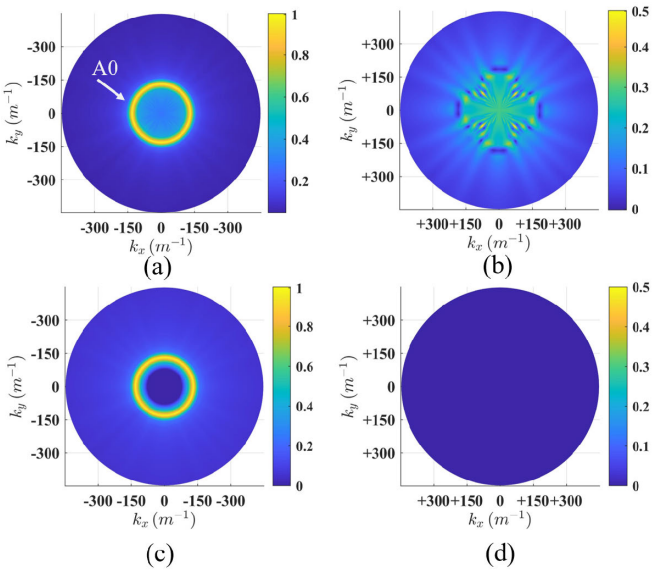

Fig. 4. Frequency-wavenumber filtering process in the polar coordinate: (a) negative wavenumber of the incident wave, (b) positive wavenumber of the reflected wave, (c) filtered wavenumber of the incident wave, and (d) filtered wavenumber of the reflected wave.

The results of the frequency-wavenumber filtering process for the wavefield in a polar grid recorded in the numerical simulation are presented in Fig. 4. In this case, the matrix of the wavefield in the polar coordinate (φ, r, t) has the size of $360 \times 75 \times 1200$ with equally spaced values. These results are depicted for the central excitation frequency. The amplitudes of all figures are normalized. Considering the steps of the proposed filtering technique, Fig. 4(a) shows the negative wavenumber results for the incident wave, whereas Fig. 4(b) indicates the positive wavenumber results for reflections propagating in the opposite direction of the incident wave propagation. As can be seen for the incident wave, the dominant mode is A0, and the amplitudes of S0 and A1 modes, which are presented in the corresponding frequency, are almost invisible. To filter out the uninteresting modes and the reflected waves,

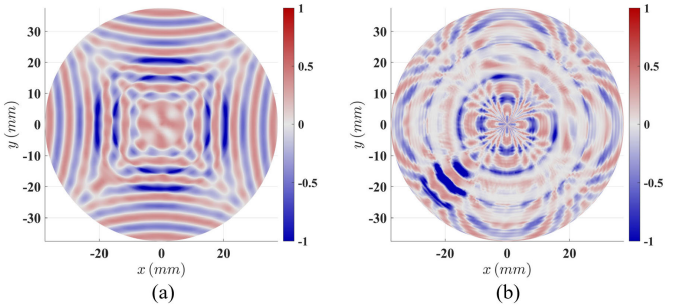

Fig. 5. Normalized wavefields at a time instant $t = 44.75\ \mu$s of the numerical simulation: (a) unfiltered data and (b) frequency-wavenumber filtered data.

the following 3-D matrix of the frequency-wavenumber filter is considered to multiply component-wise to the transformed wavefield in the polar coordinate

$$F(\varphi, k_r, \omega) = \begin{cases} 1, & 0 \le \omega \,\&\quad -k_{\max} \le k_r \le -k_{\min} \\ 1, & 0 > \omega \,\&\quad k_{\min} \le k_r \le k_{\max} \\ 0, & \text{otherwise.} \end{cases} \tag{6}$$

Note that the second line of the above equation for $0 > \omega$, is applied to meet the symmetric properties of the FFT. The filtered results in the wavenumber domain shown in Fig. 4(c) and (d) are obtained for incident and reflection waves, respectively. For this, the data is filtered by using $k_{\min} = 100\ \text{m}^{-1}$ and $k_{\max} = 447\ \text{m}^{-1}$ and ensuring the retrieval of the single A0 mode. The latter value is the maximum wavenumber obtained with the considered grid size.

After applying the frequency-wavenumber filtering process, the resulting 3-D matrix is transformed back to the time and spatial domain using the inverse 2-D FFT. Fig. 5 shows a comparison between the wavefield results at time $t = 44.75\ \mu$s for both filtered and unfiltered data. The wavefield results for unfiltered data in Fig. 5(a) clearly show that the incident and reflected waves are overlapping, and imaging using the energy of the signal is difficult. On the other hand, the filtered wavefield results presented in Fig. 5(b) indicate the concentration of the energy in the disbond region. In the next part, different features are presented to construct the damaged images using the filtered signals.

To visually understand the difference between the proposed method in the polar coordinate and the method in the Cartesian coordinate, the filtering process in the Cartesian coordinate used in [35] is also presented here. For this purpose, the same finite element model is used, and the wavefield data are recorded in the square with a side length of 75 mm, which is equal to the diameter of the scan area used for the processing in the polar coordinate. The Cartesian coordinate grid with the size of ($\Delta x = 0.5$ mm, $\Delta y = 0.5$ mm) is considered. This makes the matrix of the wavefield in the Cartesian coordinate (x, y, t) with the size of $150 \times 150 \times 1200$ an equally spaced Cartesian grid. After applying the 3-D FFT to the matrix of data in the Cartesian coordinate, the amplitudes of waves are computed in the frequency-wavenumber domain for the central excitation frequency, as shown in Fig. 6(a). As can be seen from this image, as the wavenumber values of

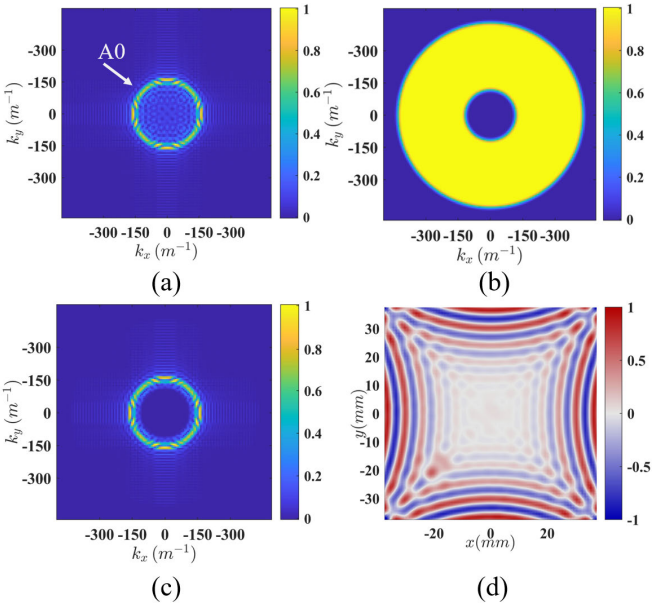

Fig. 6. Frequency-wavenumber filtering process in the Cartesian coordinate: (a) amplitudes in wavenumber domain, (b) filter mask, (c) filtered amplitudes in wavenumber domain, and (d) corresponding filtered wavefield.

incident and reflected waves are the same, the corresponding amplitudes are superimposed. Nevertheless, it is possible to retrieve only the A0 mode and filter out the modes with lower wavenumbers by using the filter mask with the same bandwidth of wavenumbers used for the polar coordinate. This filter mask is shown in Fig. 6(b). Using this filter mask, the filtered amplitudes in the frequency-wavenumber domain are obtained, and the result for the central excitation frequency are presented in Fig. 6(c). Applying the inverse 3-D FFT to the filtered data, the corresponding wavefield in the Cartesian coordinate is obtained, as illustrated in Fig. 6(d) for the same time instant as presented in Fig. 5. Using the 3-D FFT and the frequency-wavenumber filtering process in the Cartesian coordinate, it was not possible to remove the reflection from the wavefield, and as a result, the disbond could not be found.

C. Damage Imaging

A group of methods to construct the damage imaging using full wavefield is dedicated to the comparison of a feature between all data points of the scanned area. In the current study, two features are considered for damage imaging of adhesively bonded plates with isotropic and quasi-isotropic properties. These features are adapted due to the properties of the polar coordinates. The constructed images from the features have the same size as the polar coordinate grids defined as $\text{Img}(\varphi, r)$. In this way, two adapted features of RMS* and Euclidean distance (ED*) are presented.

The adapted feature RMS* is calculated based on the assumption that all inspection points in the polar grid coordinate (φ_j, r_i), have signals like those of the corresponding points $(\varphi_m, r_i), m = 1, \ldots, M$ in the circle with radius r_i from the center. Here, M is the total number of line inspections with different angles from the center. Therefore, from the conventional RMS value of time signals for each point, the

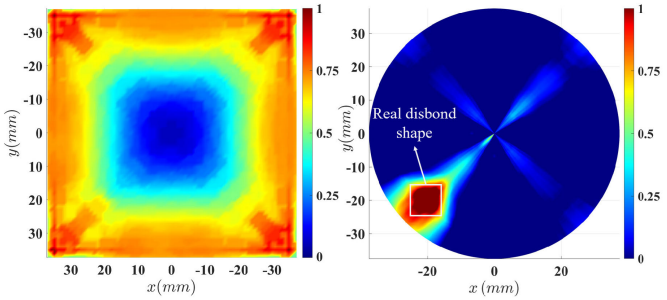

Fig. 7. Final imaging map using numerical simulation data: (a) result based on RMS values in the Cartesian coordinate and (b) result based on RMS* values in the polar coordinate.

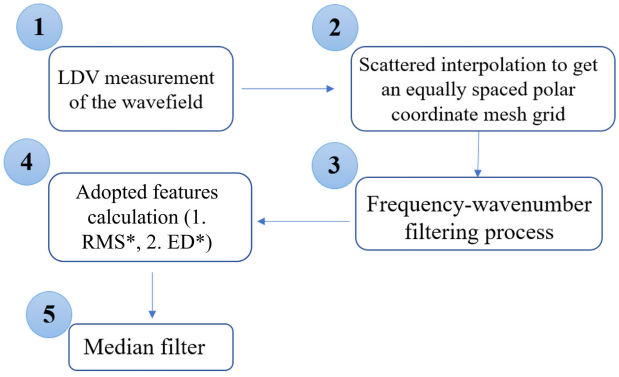

Fig. 8. Flowchart of the complete steps for the proposed damage imaging technique of adhesively bonded plates.

mean value of RMS values for all corresponding points with the same r_i is subtracted. The equation of the adapted RMS* is presented as follows:

$$\mathrm{RMS}(\varphi_j, r_i) = \sqrt{\frac{1}{N}\sum_{k=1}^{N}\left(v_{\mathrm{polar}}(\varphi_j, r_i, t_k)\right)^2}$$

$$\mathrm{RMS}^*(\varphi_j, r_i) = \mathrm{RMS}(\varphi_j, r_i) - \frac{1}{M}\sum_{m=1}^{M}\mathrm{RMS}(\varphi_m, r_i) \quad (7)$$

where, N is the length of the signals. Using the same assumption for each point in the polar coordinate, the adapted ED* is proposed by comparing the signal on each point in polar coordinates $v_{\mathrm{polar}}(\varphi_j, r_i, t_k)$ to the mean of all points with a different angle φ_j in the corresponding radius r_i from the center. Using this assumption, the following equation is presented:

$$\mathrm{ED}^*(\varphi_j, r_i) = \sqrt{\sum_{k=1}^{N}\left[v_{\mathrm{polar}}(\varphi_j, r_i, t_k) - \frac{1}{M}\sum_{m=1}^{M} v_{\mathrm{polar}}(\varphi_m, r_i, t_k)\right]^2}. \quad (8)$$

The final imaging result from numerical simulation data using both Cartesian and polar coordinates are depicted in Fig. 7(a) and (b), respectively. Note that amplitude values are mapped to the interval (0, 1) by subtracting the minimum energy from all the image points in the scanned area. The image in Fig. 7(a) is obtained by computing the RMS values of the signals. Because of the overlapping of amplitudes in the frequency-wavenumber domain for the Cartesian coordinate, the disbond could be detected. On the other hand, Fig. 7(b), which is obtained by calculation of RMS*, shows a clear indication of the disbond at its real position as defined in the simulation. Moreover, the disbond size can be retrieved quite accurately by picking the maximum rms* value of 1. Apart from the highest value of RMS* in the disbond area, there are high energy values in the vicinity of the disbond that occurred due to the scattered wave from the damage.

As the numerical simulation results are expected to have negligible noise values, the damaged image is directly obtained from the feature calculation. For experimental measurements using the 3-D LDV system, to reduce the influence of the noise, a median filter is, however, applied to the calculated features before imaging.

In summary, the damage imaging process of adhesively bonded plates using the LDV measurements and polar coordinate properties is depicted as a flowchart shown in Fig. 8. In the first step, the LDV measurements are conducted on the area of interest. In the second step, the full wavefield data is transformed into a polar coordinate mesh grid by applying the scatted interpolation function. If one is only interested in data evaluation in polar coordinates and the setup supports an equally spaced polar coordinate grid centered on the transducer, one can measure directly in polar coordinates instead of using steps 1 and 2. In the third step, frequency-wavenumber filtering is applied to remove reflections and obtain the mode of interest. In the fourth step, the two features are calculated for the filtered data to get images of the plate, and finally, in the fifth step, a median filter is applied to the images to reduce noise.

III. Experimentation and Measurements

In this section, the two adhesively bonded specimens with artificial disbonds, as well as experimental set-ups used to obtain the wavefield data from the LDV measurements, are described in detail.

A. Specimens

Two adhesively bonded samples have been fabricated, including bonded CFRP plates and bonded aluminum plates. The aluminum plates are made of aluminum 1050, and the CFRP composite plates are high-strength carbon fiber sheets produced by *Eeasycomposites* (product code = CFS-RI-1-0056). To bond the plates, Araldite 2011, which is a two-component room-temperature curing epoxy adhesive, was used. Both aluminum and CFRP plates have a thickness of 1 mm. Edge trims, with a constant thickness of 0.7 mm, are used to ensure that the bond line thickness is uniform across the bonded zone. The adhesive parts were mixed and applied in accordance with the datasheet's instructions [41]. The whole bonding zone was under continuous pressure through a vacuum bagging process. For both samples, artificial disbonds are introduced by Teflon films with a squared shape and side

Fig. 9. Fabrication of adhesively bonded aluminum plate: (a) adhesive with artificial disbond using Teflon films and (b) vacuum bagging technique.

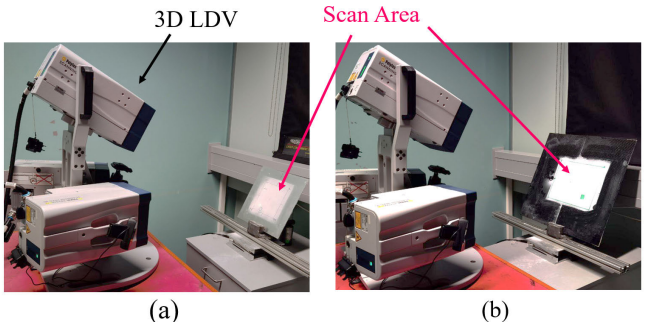

Fig. 10. 3-D LDV measurement set-up of the bonded specimens: (a) adhesively bonded aluminum specimen and (b) adhesively bonded CFRP plate.

size of 15 mm. The aluminum plates and CFRP plates have the size of 300 × 300 mm^2 and 500 × 470 mm^2, respectively. Fig. 9 shows, as an example, the fabrication of the bonded aluminum plate specimen.

B. Measurements

The wavefield measurements are conducted by using *DuraAct* piezoelectric transducers (P-876K025, *PI Ceramics*) with an active diameter of 7 mm for the UGWs excitation. The single transducer was glued to the center of each sample from the side opposite to the surface on which the wavefield measurements were carried out. The wavefield was recorded using a 3-D scanning LDV (PSV-500-3D-HV, *Polytec*). The experimental set-up for both the bonded aluminum specimen and the bonded CFRP plate is shown in Fig. 10(a) and (b), respectively. The same excitation is used for both specimens, namely a five-cycle burst, which is generated by using a function generator (TG5011, *AIM-TTI Instruments*) and a high-voltage amplifier (HVA-400-A, *Ciprian*) to amplify the signal to 150 V. A reflective spray is applied to the scan areas to ensure the diffuse reflection. The scan area for the bonded CFRP plate was approximately 240 × 240 mm^2 at the center of the plate with a Cartesian grid resolution of approximately 1.03 × 1.03 mm^2. The excitation was considered a five-cycle Hanning windowed sinusoidal burst with a central frequency of 200 kHz. This central frequency was chosen to ensure a smaller number of modes in the wavefield. The sampling frequency of the recorded signal was 6.25 MHz with a total number of points of 2500. For each position in the grid, this corresponds to a total time of acquired signals of 399.8 μs. For the bonded aluminum specimen, the scan area at the center of the plate was considered to be approximately 150 × 150 mm^2, consisting of a Cartesian grid resolution of approximately 0.79 × 0.79 mm^2. The central frequency of the excitation for the bonded aluminum plate was considered as 100 kHz. The sampling frequency, the total number of points, and the corresponding total time of the acquired signals were the same as those of the bonded CFRP specimen. For all the measurements, the Nyquist sampling theorem is respected. To increase the signal-to-noise ratio, several time signal averages were conducted at every single spatial point.

IV. Results and Discussions

To carry out the analysis of the wavefields from the 3-D recorded signals for both specimens, only the out-of-plane velocity was used for signal processing and damage imaging. In this section, the results of the signal processing and damage imaging for the measured samples are presented.

A. Adhesively Bonded Aluminum Plate

The wavefield acquired in the Cartesian coordinate gird $v(x, y, t)$ for the bonded aluminum plate was a matrix of size 189 × 191 × 2500. The wavefield data from the Cartesian grid is transformed into the wavefield in the polar coordinate grid $v_{\text{polar}}(\varphi, r, t)$, making a matrix with a size of 721 × 72 × 2500. This corresponds to an equally spaced polar coordinate grid with a resolution of 0.96 mm in $\bar{R}$ axis and 0.5° in $\bar{\phi}$ axis to cover the entire circular scanned area. The transformation is carried out by the "scattered interpolant" function of MATLAB. Based on the steps of the proposed damage imaging and signal processing techniques presented in Fig. 8, the frequency-wavenumber filtering process is applied to the obtained data. In this way, by applying the 2-D FFT to the last two dimensions of $v_{\text{polar}}(\varphi, r, t)$, the wavenumber results are obtained for different grid lines in r-axis direction for each angle φ. This leads to the separation of the wavenumber into positive and negative values. The wavenumber estimation for unfiltered wavefield at the central frequency (100 kHz) is depicted for incident waves with negative values in Fig. 11(a) and reflected waves with positive values in Fig. 11(b). The circular filter mask with $k_{\text{min}} = 75$ m^{-1} and $k_{\text{max}} = 235$ m^{-1}, which is the maximum wavenumber value of the data, is used for the incident wave. All amplitudes with positive wavenumber are removed. These filtered results are shown in Fig. 11(c) and (d) for the incident and reflected waves, respectively. It should be noted that from Fig. 11(a), the wavenumber of the A0 mode is about 82 m^{-1}, which corresponds to the wavelength of about 12.12 mm. This wavelength is smaller than the size of the artificial disbond in the aluminum specimen.

The filtered data is transformed back by using inverse 2-D FFT and the comparison of the normalized wavefield (amplitudes between 1 and 1) at time $t = 113.92$ μs for unfiltered and filtered data is presented in Fig. 12. The wavefield in Fig. 12(a) shows the combination of different modes and reflections with the high nonuniform distribution of amplitudes over the scan area. The result of the filtered wavefield in Fig. 12(b) shows a single A0 mode concentrated at and around the artificial disbond in the bonded aluminum

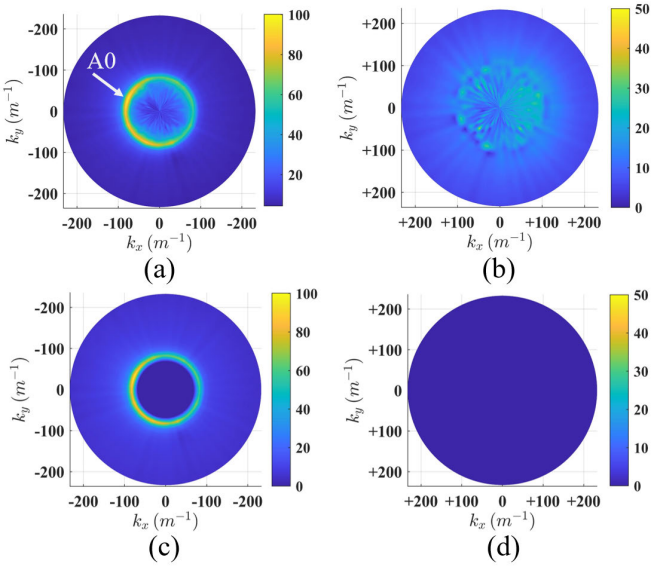

Fig. 11. Frequency-wavenumber filtering process on the 3-D LDV measurements for the bonded aluminum plate: (a) negative wavenumber of the incident wave, (b) positive wavenumber of the reflected wave, (c) filtered wavenumber of the incident wave, and (d) filtered wavenumber of the reflected wave.

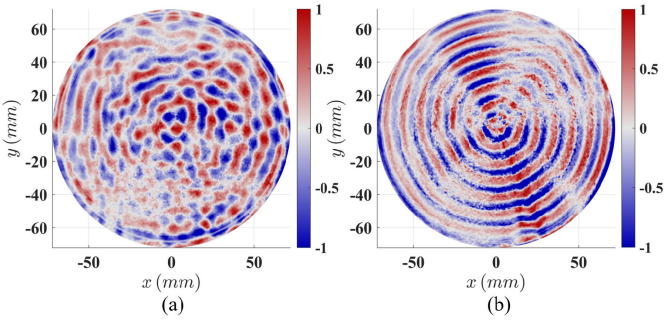

Fig. 12. Normalized wavefields measured by 3-D LDV at time $t = 113.92\ \mu$s on the adhesively bonded aluminum specimen: (a) unfiltered wavefield and (b) filtered wavefield.

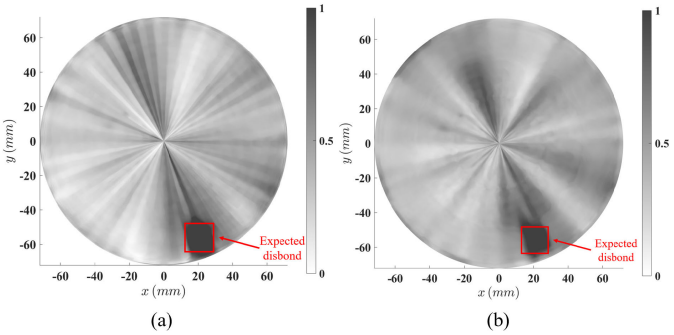

Fig. 13. Damage imaging results of the 3-D LDV measurement on the bonded aluminum plate using (a) RMS* and (b) ED*.

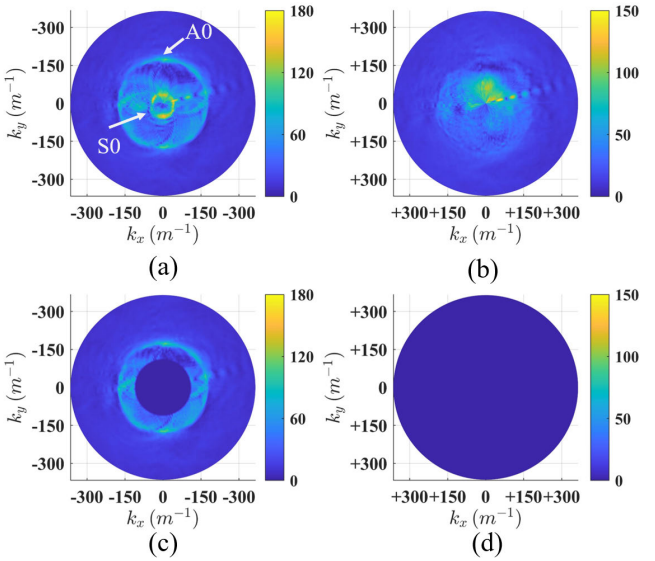

Fig. 14. Frequency-wavenumber filtering process on the 3-D LDV measurements for the bonded CFRP plate: (a) negative wavenumber of the incident wave, (b) positive wavenumber of the reflected wave, (c) filtered wavenumber of the incident wave, and (d) filtered wavenumber of the reflected wave.

plate. By using the filtered data, the features are calculated based on (7) and (8). Finally, a median filter with a filter window width of 5 mm is used to reduce the noise of the images. The images of the bonded aluminum plate using the proposed process and different features are depicted in Fig. 13. Both images obtained from the adapted features RMS* and ED* in Fig. 13(a) and (b), respectively, show an acceptable resolution of the disbond. The ED* demonstrates a slightly better resolution as the squared shape of the artificial disbond is preserved. The amplitudes of both images in Fig. 13 are subtracted from their corresponding minimum amplitude and then normalized.

B. Adhesively Bonded CFRP Plate

In the case of the adhesively bonded CFRP plate, the recorded wavefield signal in the Cartesian coordinate grid $v(x, y, t)$ was a matrix with the size of $243 \times 245 \times 2500$. The data transformed to the equally spaced polar coordinate grid with a resolution of approximately 0.67 mm in r-axis and 0.5° in φ-axis. Applying the 2-D FFT to the last two dimensions of $v_{\text{polar}}(\varphi, r, t)$, the wavenumber results are depicted for the negative and positive wavenumbers at the central frequency of 200 kHz in Fig. 14(a) and (b), respectively. The former figure shows all waves in the direction of the incident wave, and the latter figure shows all waves in the opposite direction. Compared to the same results obtained for the bonded aluminum plate, a small nonisotropy can be noticed for the modes (an elliptical shape of wavenumber distribution in the y-direction). This is because the CFRP plate used in this study is quasi-isotropic and not isotropic. Another note to be mentioned here is the amplitudes of the S0 mode, which are higher than those of the A0 mode, while for the bonded aluminum plate, it was the other way around. This is expected as by increasing the frequency of UGWs, the amplitude of the modes shows inverted parabola shapes, and the maximum amplitude of the A0 mode happens at a lower frequency compared to that of the S0 mode [42]. The anisotropy behavior of the bonded CFRP specimen is small and thus neglected. Therefore, a circular filter mask with $k_{\text{min}} = 120\ \text{m}^{-1}$ and $k_{\text{max}} = 365\ \text{m}^{-1}$ was applied to the negative wavenumber part, and all amplitudes with positive wavenumber values were suppressed to be zero.

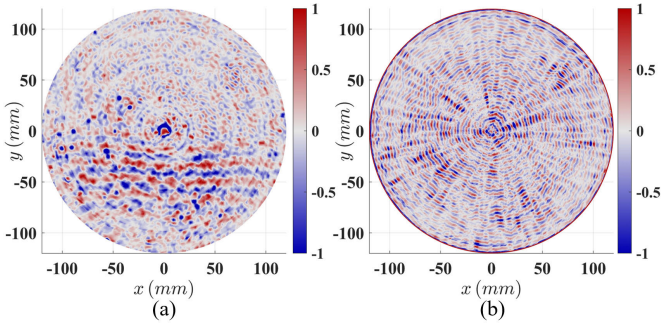

Fig. 15. Normalized wavefields measured by 3-D LDV at a time instant $t = 176.32\ \mu s$ on the adhesively bonded CFRP specimen: (a) unfiltered wavefield and (b) frequency-wavenumber filtered wavefield.

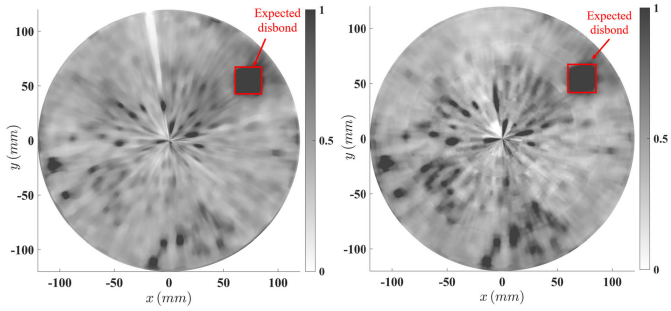

Fig. 16. Damage imaging results of the 3-D LDV measurement on the bonded CFRP plate using (a) RMS* and (b) ED*.

For the case of higher anisotropy behavior, a more complex filter mask could be designed. Using the current filter, only the A0 mode that is more sensitive to disbonds remains, and all reflected waves are removed. The filtered wavenumber amplitudes in the case of the bonded CFRP plate are shown in Fig. 14(c) and (d) for the incident and reflected waves, respectively. From Fig. 14(a), the wavenumber of the A0 mode is about 174 m^{-1}, which corresponds to the wavelength of 5.7 mm. Note that the wavelength is smaller than the size of the disbond.

Using the inverse 2-D FFT, the filtered data is transformed back to the temporal and spatial domain. Fig. 15 shows a comparison of the wavefield in the bonded CFRP specimen, with and without frequency-wavenumber filtering at a time instant $t = 176.32\ \mu s$. The amplitude of wavefields is normalized between -1 and $+1$. Fig. 15(a) corresponds to the wavefield without filtering and shows the combination of different modes and reflections with a nonuniform distribution of energy, especially from the lower area of the scanned region. This shows that the specimen is not quite uniform. On the other hand, the filtered wavefield shown in Fig. 15(b) has a single A0 mode. The same features computed for the bonded aluminum plate are used for the filtered wavefield of the bonded CFRP plate. The median filter used for the images of the bonded CFRP plate also has a filter window width of 5 mm.

The damage images of the bonded CFRP specimen obtained from calculating the adapted features and the proposed technique are presented in Fig. 16. Considering the images in this figure, the results of damage imaging using both features show the disbond shape with different resolutions. The artificial Teflon film used in the interface of the adhesive and the adherend has a squared shape, using RMS* and ED* features for Fig. 16(a) and (b), respectively, leading to a high resolution.

Comparing the imaging results for the CFRP specimen in Fig. 16 with those of the aluminum sample in Fig. 13, more details were obtained for the CFRP specimen. In both images of Fig. 16, there are several small regions with a high-intensity amplitude, which persisted even after applying the median filter. These regions correspond to unintentional voids produced during the fabrication of the sample. In general, it is assumed that waves with a smaller wavelength can detect smaller damages. The reason for accessibility to more details in the CFRP sample may be due to the wavelength of the A0 mode in both bonded specimens. Exciting the piezoelectric transducer (PZT) transducer with the same central frequency led to the propagation of A0 modes with different wavelengths in CFRP and aluminum plates due to their different mechanical properties. In the CFRP and aluminum specimens, the wavelengths of the A0 mode are about 5.7 and 12.12 mm, respectively. These values are obtained from Figs. 11(a) and 14(a), considering that the wavelength of a mode is the inverted value of the wavenumber. Also, damages smaller than the wavelength at the central frequency can be detected due to the broadband characteristic of the response signals in the frequency spectrum. Therefore, it is possible to detect defects with a size smaller than the wavelength of the central frequency of the excitation. The amplitudes of all the images in Fig. 16 are normalized after subtraction from their corresponding minimum amplitude.

V. Conclusion

In this study, a signal processing and damage imaging technique was proposed by taking advantage of the properties of the polar coordinates for the integrity assessment of the bonded region. In this approach, a single excitation source was located at the center of the scan area, and wavefields were recorded by a 3-D scanning LDV on a Cartesian mesh grid. The wavefield data was transformed into a polar coordinate mesh grid with an equally spaced mesh through a Delaunay triangulation of the scattered sample points. This transformation provides two advantages: 1) retrieval of a single mode of interest, sensitive to the damage and removing all other modes, as well as reflected waves by using the frequency-wavenumber filtering method, and 2) as, in quasi-isotropic and isotropic plates, the wave propagation behavior in all directions with different angles is expected to be similar, the potential of comparison in a radial sweep way is provided for damage imaging.

For the bonded plates used in the current study, the single A0 mode, which is more sensitive to disbonds, was retrieved through the frequency-wavenumber filtering. Adapted features, including RMS$*$, and ED$*$ were calculated to reconstruct damaged images of disbonds. Numerical modeling and experiments were successfully conducted to support the proposed method's performance in imaging the disbonds.

REFERENCES

[1] G. M. F. Ramalho, A. M. Lopes, and L. F. M. Silva, "Structural health monitoring of adhesive joints using Lamb waves: A review," *Struct. Control Health Monitor.*, vol. 29, no. 1, p. e2849, Jan. 2022, doi: 10.1002/stc.2849.

[2] K. Zhang and Z. Zhou, "Quantitative characterization of disbonds in multilayered bonded composites using laser ultrasonic guided waves," *NDT & E Int.*, vol. 97, pp. 42–50, Jul. 2018, doi: 10.1016/j.ndteint.2018.03.006.

[3] B. Yılmaz and E. Jasiūnienė, "Advanced ultrasonic NDT for weak bond detection in composite-adhesive bonded structures," *Int. J. Adhes. Adhesives*, vol. 102, Oct. 2020, Art. no. 102675, doi: 10.1016/j.ijadhadh.2020.102675.

[4] R. Zhang, M. Wan, and W. Cao, "Parameter measurement of thin elastic layers using low-frequency multi-mode ultrasonic Lamb waves," *IEEE Trans. Instrum. Meas.*, vol. 50, no. 5, pp. 1397–1403, 2001, doi: 10.1109/19.963216.

[5] R. P. Dalton, P. Cawley, and M. J. S. Lowe, "The potential of guided waves for monitoring large areas of metallic aircraft fuselage structure," *J. Nondestruct. Eval.*, vol. 20, no. 1, pp. 29–46, 2001, doi: 10.1023/A:1010601829968.

[6] B. Feng, D. J. Pasadas, A. L. Ribeiro, and H. G. Ramos, "Locating defects in anisotropic CFRP plates using ToF-based probability matrix and neural networks," *IEEE Trans. Instrum. Meas.*, vol. 68, no. 5, pp. 1252–1260, May 2019, doi: 10.1109/TIM.2019.2893701.

[7] Q. Wang, Y. Xu, Z. Su, M. Cao, and D. Yue, "An enhanced time-reversal imaging algorithm-driven sparse linear array for progressive and quantitative monitoring of cracks," *IEEE Trans. Instrum. Meas.*, vol. 68, no. 10, pp. 3433–3445, Oct. 2019, doi: 10.1109/TIM.2018.2879071.

[8] D. J. Pasadas, M. Barzegar, A. L. Ribeiro, and H. G. Ramos, "Locating and imaging fiber breaks in CFRP using guided wave tomography and eddy current testing," *Sensors*, vol. 22, no. 19, p. 7377, Sep. 2022, doi: 10.3390/s22197377.

[9] J. Rus et al., "Qualitative comparison of non-destructive methods for inspection of carbon fiber-reinforced polymer laminates," *J. Compos. Mater.*, vol. 54, no. 27, pp. 4325–4337, Nov. 2020, doi: 10.1177/0021998320931162.

[10] F. Schadow, D. Brackrock, M. Gaal, and T. Heckel, "Ultrasonic inspection and data analysis of glass- and carbon-fibre-reinforced plastics," *Proc. Struct. Integrity*, vol. 7, pp. 299–306, Jan. 2017, doi: 10.1016/j.prostr.2017.11.092.

[11] P. Van Neer, A. Volker, A. Berkhoff, T. Schrama, H. Akkerman, A. Van Breemen, L. Peeters, J.-L. van der Steen, and G. Gelinck, "Development of a flexible large-area array based on printed polymer transducers for mid-air haptic feedback," in *Proc. Meetings Acoust.*, 2019, vol. 38, no. 1, Art. no. 045008, doi: 10.1121/2.0001068.

[12] M. Thelen, N. Bochud, M. Brinker, C. Prada, and P. Huber, "Laser-excited elastic guided waves reveal the complex mechanics of nanoporous silicon," *Nature Commun.*, vol. 12, no. 1, p. 3597, Jun. 2021, doi: 10.1038/s41467-021-23398-0.

[13] K. Balasubramaniam, P. Fiborek, D. Ziaja, M. Jurek, M. Sawczak, R. Soman, and P. H. Malinowsk, "Global and local area inspection methods in damage detection of carbon fiber composite structures," *Meas. J. Int. Meas. Confed.*, vol. 187, Jan. 2022, Art. no. 110336, doi: 10.1016/j.measurement.2021.110336.

[14] T. Gao, H. Sun, Y. Hong, and X. Qing, "Hidden corrosion detection using laser ultrasonic guided waves with multi-frequency local wavenumber estimation," *Ultrasonics*, vol. 108, Dec. 2020, Art. no. 106182, doi: 10.1016/j.ultras.2020.106182.

[15] K. Pawel et al., "Dataset on full ultrasonic guided wavefield measurements of a CFRP plate with fully bonded and partially debonded Omega stringer," *Data Brief*, vol. 42, Jun. 2022, Art. no. 108078, doi: 10.1016/j.dib.2022.108078.

[16] H. Sohn, D. Dutta, J. Y. Yang, M. DeSimio, S. Olson, and E. Swenson, "Automated detection of delamination and disbond from wavefield images obtained using a scanning laser vibrometer," *Smart Mater. Struct.*, vol. 20, no. 4, Apr. 2011, Art. no. 045017, doi: 10.1088/0964-1726/20/4/045017.

[17] Z. Tian, S. Howden, Z. Ma, W. Xiao, and L. Yu, "Pulsed laser-scanning laser Doppler vibrometer (PL-SLDV) phased arrays for damage detection in aluminum plates," *Mech. Syst. Signal Process.*, vol. 121, pp. 158–170, Apr. 2019, doi: 10.1016/j.ymssp.2018.11.016.

[18] S. Majhi, A. Mukherjee, N. V. George, V. Karaganov, and B. Uy, "Corrosion monitoring in steel bars using laser ultrasonic guided waves and advanced signal processing," *Mech. Syst. Signal Process.*, vol. 149, Feb. 2021, Art. no. 107176, doi: 10.1016/j.ymssp.2020.107176.

[19] M. Mitra and S. Gopalakrishnan, "Guided wave based structural health monitoring: A review," *Smart Mater. Struct.*, vol. 25, no. 5, May 2016, Art. no. 053001, doi: 10.1088/0964-1726/25/5/053001.

[20] E. Glushkov, N. Glushkova, M. V. Golub, J. Moll, and C.-P. Fritzen, "Wave energy trapping and localization in a plate with a delamination," *Smart Mater. Struct.*, vol. 21, no. 12, Dec. 2012, Art. no. 125001, doi: 10.1088/0964-1726/21/12/125001.

[21] B. Park, Y.-K. An, and H. Sohn, "Visualization of hidden delamination and debonding in composites through noncontact laser ultrasonic scanning," *Compos. Sci. Technol.*, vol. 100, pp. 10–18, Aug. 2014, doi: 10.1016/j.compscitech.2014.05.029.

[22] Y.-K. An, B. Park, and H. Sohn, "Complete noncontact laser ultrasonic imaging for automated crack visualization in a plate," *Smart Mater. Struct.*, vol. 22, no. 2, Feb. 2013, Art. no. 025022, doi: 10.1088/0964-1726/22/2/025022.

[23] E. Wojtczak and M. Rucka, "Wave frequency effects on damage imaging in adhesive joints using Lamb waves and RMS," *Materials*, vol. 12, no. 11, p. 1842, Jun. 2019, doi: 10.3390/ma12111842.

[24] J. Segers, S. Hedayatrasa, G. Poelman, W. Van Paepegem, and M. Kersemans, "Robust and baseline-free full-field defect detection in complex composite parts through weighted broadband energy mapping of mode-removed guided waves," *Mech. Syst. Signal Process.*, vol. 151, Apr. 2021, Art. no. 107360, doi: 10.1016/j.ymssp.2020.107360.

[25] T. Gao, X. Liu, J. Zhu, B. Zhao, and X. Qing, "Multi-frequency localized wave energy for delamination identification using laser ultrasonic guided wave," *Ultrasonics*, vol. 116, Sep. 2021, Art. no. 106486, doi: 10.1016/j.ultras.2021.106486.

[26] M. Radzieński, P. Kudela, A. Marzani, L. De Marchi, and W. Ostachowicz, "Damage identification in various types of composite plates using guided waves excited by a piezoelectric transducer and measured by a laser vibrometer," *Sensors*, vol. 19, no. 9, p. 1958, Apr. 2019, doi: 10.3390/s19091958.

[27] O. Mesnil, C. A. Leckey, and M. Ruzzene, "Instantaneous and local wavenumber estimations for damage quantification in composites," *Struct. Health Monitor.*, vol. 14, no. 3, pp. 193–204, May 2015, doi: 10.1177/1475921714560073.

[28] M. D. Rogge and C. A. C. Leckey, "Characterization of impact damage in composite laminates using guided wavefield imaging and local wavenumber domain analysis," *Ultrasonics*, vol. 53, no. 7, pp. 1217–1226, Sep. 2013, doi: 10.1016/j.ultras.2012.12.015.

[29] J. Segers, S. Hedayatrasa, G. Poelman, W. Van Paepegem, and M. Kersemans, "Self-reference broadband local wavenumber estimation (SRB-LWE) for defect assessment in composites," *Mech. Syst. Signal Process.*, vol. 163, Jan. 2022, Art. no. 108142, doi: 10.1016/j.ymssp.2021.108142.

[30] Y. Lugovtsova, J. Bulling, O. Mesnil, J. Prager, D. Gohlke, and C. Boller, "Damage quantification in an aluminium-CFRP composite structure using guided wave wavenumber mapping: Comparison of instantaneous and local wavenumber analyses," *NDT & E Int.*, vol. 122, Sep. 2021, Art. no. 102472, doi: 10.1016/j.ndteint.2021.102472.

[31] M. Barzegar, D. J. Pasadas, A. Lopes Ribeiro, and H. G. Ramos, "Experimental estimation of Lamb wave dispersion curves for adhesively bonded aluminum plates, using two adjacent signals," *IEEE Trans. Ultrason., Ferroelectr., Freq. Control*, vol. 69, no. 6, pp. 2143–2151, Jun. 2022, doi: 10.1109/TUFFC.2022.3164731.

[32] G. Sha, H. Xu, M. Radzieński, M. Cao, W. Ostachowicz, and Z. Su, "Guided wavefield curvature imaging of invisible damage in composite structures," *Mech. Syst. Signal Process.*, vol. 150, Mar. 2021, Art. no. 107240, doi: 10.1016/j.ymssp.2020.107240.

[33] J. Y. Jeon, D. Kim, G. Park, E. Flynn, T. Kang, and S. Han, "2D-wavelet wavenumber filtering for structural damage detection using full steady-state wavefield laser scanning," *NDT & E Int.*, vol. 116, Dec. 2020, Art. no. 102343, doi: 10.1016/j.ndteint.2020.102343.

[34] M. S. Harb and F.-G. Yuan, "Damage imaging using non-contact air-coupled transducer/laser Doppler vibrometer system," *Struct. Health Monitor.*, vol. 15, no. 2, pp. 193–203, Mar. 2016, doi: 10.1177/1475921716636336.

[35] M. Ruzzene, "Frequency–wavenumber domain filtering for improved damage visualization," *Smart Mater. Struct.*, vol. 16, no. 6, pp. 2116–2129, Dec. 2007, doi: 10.1088/0964-1726/16/6/014.

[36] S. Shoja, V. Berbyuk, and A. Boström, "Delamination detection in composite laminates using low frequency guided waves: Numerical simulations," *Compos. Struct.*, vol. 203, pp. 826–834, Nov. 2018, doi: 10.1016/j.compstruct.2018.07.025.

[37] A. Huber, "Dispersion calculator user's manual," German Aerosp. Center (DLR), Augsburg, Germany, 2019.

[38] R. Soleimanpour, C.-T. Ng, and C. H. Wang, "Higher harmonic generation of guided waves at delaminations in laminated composite beams," *Struct. Health Monitor.*, vol. 16, no. 4, pp. 400–417, Jul. 2017, doi: 10.1177/1475921716673021.

[39] L. Maio, V. Memmolo, F. Ricci, N. D. Boffa, and E. Monaco, "Investigation on fundamental modes of guided waves propagating in symmetric and nonsymmetric composite laminates," *Proc. Inst. Mech. Eng., C, J. Mech. Eng. Sci.*, vol. 231, no. 16, pp. 2988–3000, Aug. 2017, doi: 10.1177/0954406217698721.

[40] I. Amidror, "Scattered data interpolation methods for electronic imaging systems: A survey," *J. Electron. Imag.*, vol. 11, no. 2, p. 157, Apr. 2002, doi: 10.1117/1.1455013.

[41] *Huntsman Araldite 2011 Epoxy Technical Data Sheet*, Huntsman Corp., The Woodlands, TX, USA, 2015.

[42] G. B. Santoni, L. Yu, B. Xu, and V. Giurgiutiu, "Lamb wave-mode tuning of piezoelectric wafer active sensors for structural health monitoring," *J. Vib. Acoust.*, vol. 129, no. 6, pp. 752–762, Dec. 2007, doi: 10.1115/1.2748469.

Mohsen Barzegar was born in Bojnord, Iran, in 1992. He received the M.Sc. degree in aerospace engineering from Sharif University of Technology (SUT), Tehran, Iran. He is currently pursuing the Ph.D. degree in electrical and computer engineering from the IST, Universidade de Lisbon, Lisbon, Portugal.

He is also a Marie Skłodowska-Curie Early Stage Researcher at Instituto de Telecomunicações under the project of GW4SHM, focusing on damage imaging of adhesive joints using guided wave-based inspection. His research interests include but are not limited to structural health monitoring, fracture, and fatigue analysis of adhesively bonded structures, as well as composite materials.

Dario J. Pasadas was born in Geneva, Switzerland, in 1986. He received the M.Sc. degree in electronics engineering from the Instituto Superior Técnico (IST), Technical University of Lisbon, Lisbon, Portugal, in 2010, and the Ph.D. degree in electrical and computer engineering from IST, Universidade de Lisbon, Lisbon, in 2017.

He is currently a Post-Doctoral Researcher with the Instituto de Telecomunicações, Universidade de Lisbon. His current research interests include instrumentation, electronics, digital signal processing, inverse problem algorithms, and machine learning algorithms for applications in nondestructive evaluation.

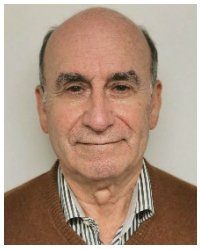

Artur L. Ribeiro was born in Lisbon, Portugal, in 1950. He received the License degree in electrical engineering (branch of telecommunications and electronics), the Ph.D. degree in electrical and computer engineering, and the Habilitation degree from the Instituto Superior Técnico (IST), Technical University of Lisbon (UTL), Lisbon, in 1973, 1990, and 2000, respectively.

In 1977, he joined the Department of Electrical and Computer Engineering, IST/UTL, where he was a Faculty Member. He has been a member of the Instituto de Telecomunicações since its foundation in 1991. His current research interests include instrumentation and electric measurements with special applications to nondestructive testing and evaluation techniques.

Helena G. Ramos received the Ing., M.Sc., Ph.D., and Habilitation degrees in electrical and computer engineering from the Instituto Superior Técnico (IST), Technical University of Lisbon, Lisbon, Portugal, in 1980, 1987, 1995, and 2005, respectively.

She is currently an Associate Professor with the IST and a Senior Researcher with the Instituto de Telecomunicações, Universidade de Lisbon, Lisbon. Her current research interests include nondestructive testing, Eddy current evaluation, ultrasound guided waves, transducers, measurement interfaces, ADC testing, and ferromagnetic materials modeling.

Dr. Ramos is the Vice-President of the IST Scientific Board from 2010 to 2017 and a member of the AdCom of the IEEE Instrumentation and Measurement Society.

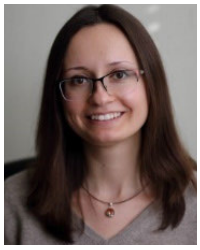

Yevgeniya Lugovtsova was born in Ust-Kamenogorsk, Kazakhstan, in 1991. She received the bachelor's degree in instrument making from East State Kazakhstan Technical University, Oskemen, in 2013 and the dual master's degree in nondestructive testing from Dresden International University, Dresden, Germany, and Tomsk Polytechnic University, Tomsk, Russia, in 2016.

Since 2016, she has been working as a Research Associate at Acoustic and Electromagnetic Methods Division, Bundesanstalt für Materialforschung und–prüfung (BAM), Berlin, Germany. Her research mainly focuses on ultrasonic-guided waves and their application to material characterization and structural health monitoring.

Jannis Bulling was born in 1989, in Berlin, Germany. He received the master's degree in science and mathematics from the Free University of Berlin, Berlin, in 2016.

Since 2016, he has been working as a Research Associate at the Acoustic and Electromagnetic Methods Group, Federal Institute for Materials Research and Testing (BAM), Berlin. His research focuses on numerical methods, inverse problems, and signal processing for nondestructive evaluation and structural health monitoring with ultrasound guided waves.